1 **Long-range transport of Asian dust to the Arctic:**

2 **identification of transport pathways, evolution of**

3 **aerosol optical properties, and impact assessment on**

4 **surface albedo changes**

6 **Xiaoxi Zhao[1], Kan Huang[1,3,4*], Joshua S. Fu[2]**

7 [1]Center for Atmospheric Chemistry Study, Shanghai Key Laboratory of Atmospheric Particle

8 Pollution and Prevention (LAP[3]), Department of Environmental Science and Engineering, Fudan

9 University, Shanghai, 200433, China

10 [2]Department of Civil and Environmental Engineering, University of Tennessee, Knoxville, TN,

11 USA

12 [3]IRDR ICoE on Risk Interconnectivity and Governance on Weather/Climate Extremes Impact and

13 Public Health, Fudan University, Shanghai 200433, China

14 [4]Institute of Eco-Chongming (IEC), Shanghai, 202162, China

15 **Corresponding author:** huangkan@fudan.edu.cn

17 **Abstract**

18 Airborne dust is one of the most important natural aerosols, it has various

19 environmental impacts on air quality, ocean fertilization, and the global climate change.

20 Asian dust, representing one of the major dust sources in the world, has been widely

21 studied due to its long-range transport capability. However, its transport to the Arctic

22 has been less investigated. In this study, two typical transport routes were identified

23 based on the recorded dust events in China during 2011-2015. Accordingly, two specific

24 Asian dust long-range transport events were selected and compared, i.e., one observed

25 at Barrow, Alaska (travelled mostly over lands within 6-7 days) and the other one

26 observed at Alert, Canada (travelled mostly over oceans within 7-8 days). The transport

27 routes of the two dust events had been cross-validated by using air mass trajectory

28 modeling, meteorology reanalysis data, ground-based aerosol columnar and profiling

29 observations, and spaceborne remote sensing. It was found that different transport

30 routes to the Arctic had divergent effects on the evolution of aerosol properties,

31 revealing different mixing extents between dust, anthropogenic particles, smoke, and

32 sea salts. Based on the SNow ICe Aerosol Radiative model, the albedo simulation

33 indicated that dust and elemental carbon together reduced the surface albedo by 0.35%

34 to 2.63% compared to the pure snow condition. This study implied that the dust long-

35 transport from China to the Arctic was ubiquitous and may be a potential contributor to

36 the Arctic regional climate and ecosystem.

38 **1. Introduction**

39 In the context of global warming, the Arctic temperature has been increasing at a rate

40 higher than the global average in recent decades, which is the so-called "Arctic

41 Amplification" effect (Serreze et al., 2009; Serreze and Francis, 2006). Although the

42 increase of greenhouse gases concentrations was an important driver of the Arctic and

43 global warming, the underlying cause of Arctic amplification remained uncertain as

44 Arctic warming and ice cap melting were also associated with changes in surface albedo,

45 aerosol radiative forcing, cloud cover, atmospheric water vapor content, seawater

46 temperature, and etc. (Screen and Simmonds, 2010; Gillett et al., 2008). The

47   magnitudes of direct radiative forcing of Arctic aerosols were closely related to the

48   origin of aerosol, transport, and deposition (Quinn et al., 2008). During the long

49   transport of aerosols to the Arctic, the solar radiation could be absorbed or scattered by

50   some components in the aerosols (black carbon, sulfate, etc.), which led to a decrease

51   of the amount of solar radiation reaching the surface. However, this cooling effect may

52   be diminished by the decrease of Arctic aerosol concentrations in recent decades

53   (Gagne et al., 2017; Breider et al., 2017). On the other hand, aerosol-radiation

54   interactions also contributed to Arctic warming in the following ways. Firstly,

55   absorbing aerosols at low latitudes could enhance the latitudinal gradient of temperature,

56   thus enhancing heat transport from other regions to the Arctic (Sand et al., 2013b; Sand

57   et al., 2013a); Secondly, absorbing aerosols absorbed solar radiation and warmed the

58   Arctic atmosphere while the surface was cooled, which enhanced atmospheric stability

59   and constrained the diffusion of air pollutants (Blanchet and List, 2010; Koch and Del

60   Genio, 2010; Brock et al., 2011); Thirdly, deposition of absorbing aerosols onto snow

61   and ice could reduce the surface albedo of the Arctic and thus led to local warming.

62   Besides, the formation of mixed-phase clouds in the Arctic were found related to low

63   concentrations and acid coating of dust particles based on both global and parcel model

64   simulations (Fan, 2013). Overall, direct and indirect radiative forcings caused by

65   aerosols had significant impacts on the Arctic climate as demonstrated by the model

66   simulation results (Shindell and Faluvegi, 2009; Flanner, 2013). In addition to the

67   impact of absorbing aerosols on the Arctic climate, the snow-albedo feedback and

68   cloud-albedo feedback in Central Siberia significantly regulated the variation of dust

69   emissions in spring over the Gobi Desert (Liu et al., 2018).

70   Due to the sparse human activities in the Arctic, most of the air pollutants

71   originated from the middle and lower latitudes, e.g., Eurasia, Siberia, North America,

72   and Southeast Asia. Eurasia was the main source area for the lower Arctic altitudes and

73   the higher Arctic altitudes was mainly influenced by South and Central Asia (Qi et al.,

74   2017; Fisher et al., 2011; Sharma et al., 2013; Stohl, 2006). Di Pierro et al. (2011) and

75   Huang et al. (2015a) both used ground-based lidar data and satellite remote sensing

76   images to demonstrate that aerosols from China can be transported to the Arctic within

77   4-6 days. Similarly, Di Biagio et al. (2018) found that aerosols in the high Arctic north

78   of Svalbard from October, 2014 to June, 2015 were mainly from Russia. Warneke et al.

79   (2010) found that forest fires in Russia strongly affected air pollutant concentrations in

80   the Arctic atmosphere and surface snowpack based on aircraft observations and

81   numerical simulation. Marelle et al. (2015) investigated a long-transport event from

82   Europe to the Arctic in April, 2008 and estimated a maximum shortwave radiation of

83   3.3 W m^{-2} at the top of the atmosphere, yielding a significant local warming effect.

84   Sobhani et al. (2018) applied the WRF-STEM (Weather Research and Forecasting -

85   sulfur transport and deposition model) model to study the long-range transport of

86   aerosols to the Arctic and calculated the contribution of various anthropogenic and

87   biomass burning emissions. Europe and China were found as the main source regions

88   of Arctic black carbon, contributing about 46% and 25% in the middle and upper

89   troposphere, respectively.

90   Different from black carbon, dust had a much larger geographic influencing

91   coverage due to that dust particles were usually accompanied with strong winds.

92   Although a number of studies focused on local or regional dust in the Arctic (Ferrero et

93   al., 2019; Ranjbar et al., 2021; Dagsson-Waldhauserova et al., 2019), the long-range

94   transport of dust to the Arctic has been frequently observed. Asian dust can be

95   transported across the Pacific Ocean to reach North America and even the Arctic (Wang

96   et al., 2018b; Guo et al., 2017). Zwaaftink et al. (2016) combined a Lagrangian particle

97   dispersion model FLEXPART (FLEXible PARTicle dispersion model) and surface

98   particle concentration observations to simulate the global dust emissions. It was

99   estimated that the dust loading in the Arctic was dominated by Asia (38%) and Africa

100   (32%) sources while the local contribution was around 27%. The instantaneous

101   radiative forcing in the Arctic caused by dust was also dominated by Asia and Africa.

102   In addition, the deposition of dust on snow was responsible for almost all of the bottom

103   of the atmosphere instantaneous radiative forcing (Kylling et al., 2018).

104   Although both observational and modeling studies showed a persistent source of

105   the Arctic dust from Asia (Fan, 2013; Ginoux et al., 2012), the transport pathways were

106   seldom explored. Huang et al. (2015b) revealed an unreported transport path of Asian

107   dust to the Arctic and estimated its transport duration. In this study, the frequency of

108   dust from China that had the capability to be transported to the Arctic was estimated.

109   Two typical dust transport pathways to the Arctic were investigated based on a synergy

110   of remote sensing data and Arctic monitoring data. The evolutions of aerosol optical

111   properties during the long-range transport were analyzed. Finally, the potential impact

112   of absorbing aerosol on the decrease of surface albedo was quantified.

113

2. Data and Methodology

2.1. Receptor sites in the Arctic

Two Arctic monitoring sites were chosen as the investigated receptors (Figure 1). One
site is Barrow (71.32°N, 156.61°W) located in the northernmost part of the Alaska
region of USA. It is surrounded by the Arctic Ocean on three sides and has a large ice
cap. Barrow is characterized of a cold and dry climate and covered by snow and ice
all year round with an average annual temperature of about -11°C (Dong et al., 2010).
In winter, the frequency of northerly air currents was high. The average surface
temperature reached as low as -25°C in January and February and most of the
snowfall occurred at the end of February. Since April, the invasion of warm and moist
air masses from the North Pacific Ocean began to prompt the snowpack in Alaska to
melt (Stone et al., 2002). This site is managed by Earth System Research Laboratory
of National Oceanic and Atmospheric Administration.

The other site is Alert (82.50°N, 62.34°W) in the Nunavut region of Canada, the
northernmost permanent human settlement in the world. This site is located about 500
km north of Greenland, near the North Pole and far from any industrial emissions. It
is very cold due to the long-lasting polar night with four months in a year. The
average temperature was below -30°C from December to March and the average
annual temperature was -17.9°C (Weijers et al., 2017). This site is managed by
Environment Canada.
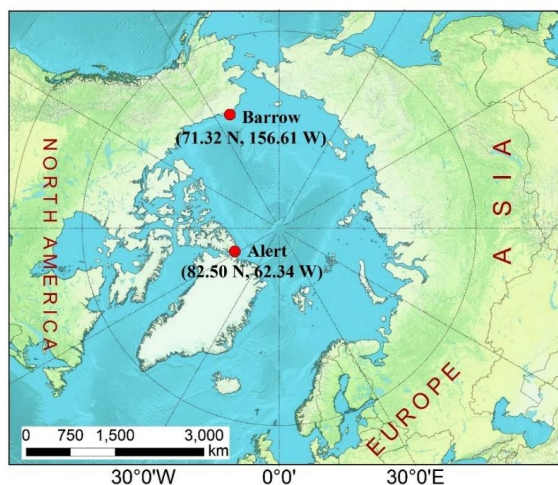
134

135   Figure 1. Two receptor sites (Barrow and Alert) in the Arctic. The map is created by

136   ArcGIS 10.2.

137

138 **2.2. Aerosol measurements**

139 Particles at Barrow and Alert were measured by the three-wavelength (450, 550, and

140 700nm) Integrating Nephelometer (Model 3563). The nephelometer measured the

141 angular integral of light scattering and Beer-Lambert Law was applied to calculate the

142 light extinction. In this study, the measurement results at 550nm were used. Aerosol

143 Robotic Network (AERONET) established a global observational network of

144 columnar aerosol optical properties based on Cimel-31 Sun Photometers (Holben et

145 al., 1998). Key parameters of aerosol optical properties were retrieved at 440 nm, 670

146 nm, 870 nm, and 1020 nm, respectively. The quality-assured level 2.0 data were used.

147 The AD-Net (Asian dust and aerosol lidar observation network) operated by National

148 Institute for Environmental Studies (NIES) established a lidar network of dual-

149 wavelength depolarization lidars (Model: L2S-SM II), aiming to obtain the four

150   dimensional distributions (sites/time/height/aerosol properties) of aerosol particles in

151   East Asia (Shimizu et al., 2017). The lidar could measure backscattering coefficients

152   and the depolarization ratio at the wavelength of 532 nm. The lidar continuously

153   operated with 15 min intervals and 30m height resolution.

154   In addition to the ground-based sites, remote sensing from space was used to

155   provide widespread spatial information of aerosols. The MODIS (Moderate-resolution

156   Imaging Spectroradiometer) Level-3 aerosol products (1° × 1°) were obtained from

157   NASA's Giovanni (https://giovanni. gsfc.nasa.gov/giovanni/). Aerosol optical depth

158   (550nm) data was based on the Dark Target and Deep Blue algorithm and Angström

159   exponent (0.412-0.47nm) data was based on the Deep Blue algorithm. The CALIOP

160   (Cloud-Aerosol Lidar with Orthogonal Polarization) Lidar onboard the CALIPSO

161   (Cloud-Aerosol Lidar and Infrared Pathfinder Satellite Observation) satellite provided

162   global data on aerosol and cloud layers with a horizontal and vertical resolution of

163   around 5km and 60m. Track scale vertical aerosol profiles were derived. In addition,

164   major aerosol subtypes can be identified, including dust, smoke, clean continental,

165   polluted continental, clean marine, and polluted dust.

166

167   **2.3. Air mass trajectories modeling**

168   To track the possible source regions of airborne particles, HYSPLIT4 (HYbrid Single-

169   Particle Lagrangian Integrated Trajectory) was run online at the NOAA (National

170   Oceanic and Atmospheric Administration) ARL (Air Resource

171   Laboratory) READY (Real-time Environmental Applications and Display sYstem)

172 Website (http://www.arl.noaa.gov/ready/hysplit4.html). The HYSPLIT model is a

173 complete system for calculating simple air mass backward trajectories, in addition to

174 dispersion and complex deposition simulations (Draxier and Hess, 1998). The

175 meteorological input data used in the model were obtained from the National Center

176 for Environmental Prediction's (NCEP) global data assimilation system (GDAS) with

177 a horizontal resolution of 0.5° x 0.5°.

178

179 **2.4. Snow albedo modeling**

180 The Snow–Ice–Aerosol–Radiative (SNICAR) model was used to simulate the impact

181 of impurity (e.g. dust, black carbon, and volcanic ash) on the surface albedo of snow

182 and ice (Flanner et al., 2007). The application of the SNICAR model required inputs

183 such as snow grain effective radius, snowpack thickness/density, surface albedo, the

184 concentrations of impurities in snow. The effective grain sizes of snow ranged from

185 100 μm for fresh clean snow to 1500 μm for aged snow and granular ice. Table 1 lists

186 the parameters considered for SNICAR in this study. The parameters of snow were

187 derived from field measurements at Barrow in April, 2015 (Dou et al., 2017) and near

188 Alert in February and April, 2000 (Domine et al., 2002). The estimation of impurities

189 concentrations in snow will be presented in Section 3.7.1.

190

191 **Table 1. The input parameters in the SNICAR model**

Parameters	Barrow	Alert
Incident radiation	Direct	
Surface spectral distribution	Summit Greenland, clear-sky	

Snow grain effective radius (μm)	180(Dou et al., 2017)	500(0.1-1.5mm)(Domine et al., 2002)
Snowpack thickness (m)	0.35(Dou et al., 2017)	0.4(Domine et al., 2002)
Snowpack density (kg/m3)	350(Dou et al., 2017)	300(Domine et al., 2002)
Albedo of underlying ground	0.73(300-700nm)0.33(700-5000nm)(Dou et al., 2017)	

192

3. Results and Discussion

3.1. Overview of dust events in China from 2011-2015

Table 2 summarizes the occurrence frequency and duration of dust events in the dust source regions of China during 2011-2015 recorded by China's Sand-dust Weather Almanac (Cma, 2013, 2014, 2015, 2016, 2017). A total of 50 dust events occurred, which were categorized into three types, i.e., floating dust, dust storm, and severe dust storm. Among them, the occurrence frequency of floating dust reached 36, accounting for 72% of the total dust events. On average, floating dust occurred about 7 times a year with a total duration of 61 days. The occurrence frequencies of dust storm and severe dust storm events were both 7 times with the total duration of 18 days. Compared with 2000-2010, the frequency of dust storm and severe dust storm events during the last five years decreased significantly, while that of floating dust increased.

Table 2. Summary of dust weather conditions in China during 2011 – 2015

Year	floating dust		dust storm		severe dust storm		Total
	frequency	days	frequency	days	frequency	days	frequency
2011	5	10	1	3	2	6	8
2012	5	10	3	8	2	4	10
2013	9	15	1	2			10

2014	4	8	1	2	2	6	7
2015	13	18	1	3	1	2	15
Total	36	61	7	18	7	18	50

207

208

209   On a seasonal basis (Table 3), the springtime (March-May) was the peak period of

210   dust outbreak in China. 41 dust events occurred, accounting for 82% of the total dust

211   events. Of which, relatively high frequencies of dust storm and severe dust storm events

212   were observed, accounting for 37.5% of the total events in April. This high frequency

213   of dust occurrence in the spring of China was mainly related to the climatic

214   characteristics, geographic conditions, and geological structure of northern China.

215   Strong winds caused by the Inner Mongolia cyclone and cold fronts in spring resulted

216   in the frequent outbreak of dusty weather in northern China. In terms of the

217   geographical dust source areas in China, the source regions of dust included the South

218   Xinjiang basin, central and western Inner Mongolia, central and western Gansu, and

219   northern Shaanxi.

220

221   **Table 3. Monthly summary of dust days in China during 2011 – 2015**

Month	floating dust	dust storm	severe dust storm	total
February	3			3
March	12	1	2	15
April	10	3	3	16
May	7	1	2	10
June	1			1
August	1			1
November	2	2		4

222

3.2 Transport pathways of Asian dust to the Arctic

224 In order to investigate the frequency and transport pathways of dust from China to the

225 Arctic, the HYSPLIT trajectory model was applied in this study. Based on the outbreak

226 time and source areas of dust recorded by China's Sand-dust Weather Almanac, 10-15

227 days forward trajectories starting at altitudes of 500m, 1000m, and 1500m were

228 computed for each dust event in China during 2011-2015. If the trajectories entered the

229 Arctic Circle (latitudes higher than 66°34'N), the specific dust event was recorded as

230 one dust long-range transport event from China to the Arctic.

231

232
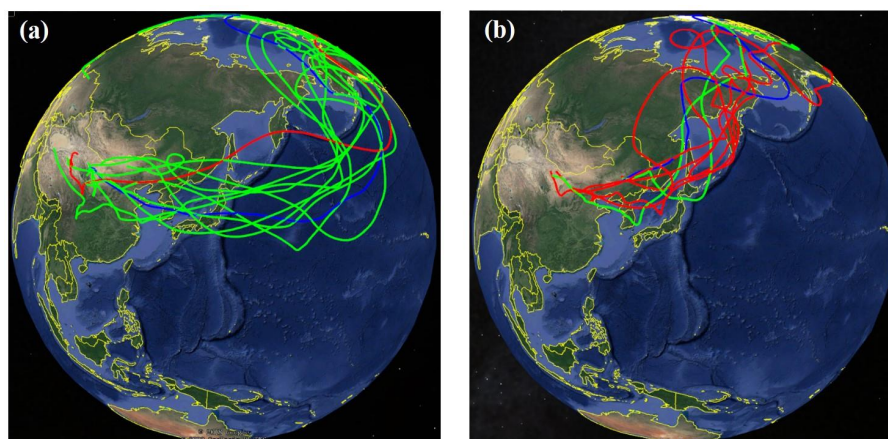
Figure 2. Two common transport pathways of dust originating from China to the Arctic, i.e., (a) the northern China - Korean Peninsula/Japan - North Pacific Ocean – Arctic pathway and (b) the northern China - Korean Peninsula/Japan - Kamchatka Peninsula - East Siberia – Arctic pathway. Red, blue, and green curves represent forward trajectories starting at altitudes of 500m, 1000m, and 1500, respectively. The map is © Google Earth 2019.

239

240 Based on this criterion, 38 out of the 50 dust events that originated from China

241 during 2011-2015 had the potential migrating to the Arctic Circle. Among these

242 identified dust events, most occurred in spring with 32 events and the transport duration

243 varied between 4 and 13 days. Two main types of dust transport from China to the

244 Arctic were distinguished in Figure 2. As for Type I (Figure 2a), dust mainly originated

245 from the central parts of Inner Mongolia and central Gansu. It passed through northern

246 China, Korean Peninsula, Japan and the North Pacific Ocean, and finally reached

247 Siberia and the northern part of Alaska. This transport type was characterized of wide

248 geographic coverage, relatively long transport duration (about 7-10 days), and mainly

249 over the open ocean. This was due to the high lifting altitude (mostly over 1500m) over

250 the dust source regions, so particles can be transported to even further areas.

251   As for Type II (Figure 2b), dust mainly originated from northeast China and

252 western Inner Mongolia, then passing over the Korean Peninsula, northern Japan,

253 Kamchatka Peninsula, and finally reaching East Siberia and its northern areas.

254 Compared to Type I, the Type II transport pathways travelled more over land and had

255 relatively shorter duration of about 4-8 days. This was due to the presence of a low-

256 pressure system over northern Japan in spring, which induced the air masses deflecting

257 northward.

258

259 **3.3 Two cases of long-range transported dust to the Arctic**

260 Figure 3a shows the time series of scattering coefficients (σ_{sp}) of PM_1 and PM_{10} at 550

261 nm at Barrow during April 17-21, 2015. The scattering coefficients stayed at low levels

262 from the early morning of April 17 to the evening of April 18, which were similar to

263   the annual average values at Barrow in 2015 (4.8 Mm^{-1} and 8.1 Mm^{-1} for PM$_1$ and PM$_{10}$,

264   respectively). Since the early morning of April 19, both σ_{sp}(PM$_1$) and σ_{sp}(PM$_{10}$)

265   climbed simultaneously, indicating the invasion of air pollutants. At 15:00 on April 19,

266   σ_{sp}(PM$_1$) reached relatively high value of 19.8 Mm^{-1} and was still close to that of PM$_{10}$

267   with the σ_{sp}(PM$_1$)/σ_{sp}(PM$_{10}$) ratio of 0.82, indicating fine particles dominated during

268   this period. Afterwards, σ_{sp}(PM$_{10}$) continued to increase until it reached the maximum

269   value of 42.2 Mm^{-1} at 4:00 on April 20, more than 5 times of its annual average. The

270   mean σ_{sp}(PM$_1$)/σ_{sp}(PM$_{10}$) ratio during 14:00, April 19 - 12:00, April 21 decreased to

271   0.47 ± 0.10, obviously indicating the enrichment of coarse particles. This episode is

272   defined as CASE I.

273   Figure 3b shows the time series of scattering coefficients of PM$_1$ and PM$_{10}$ at 550

274   nm at Alert from March 13 to 19, 2013. The annual average σ_{sp}(PM$_1$) and σ_{sp}(PM$_{10}$)

275   at Alert was 4.2 Mm^{-1} and 6.0 Mm^{-1}, respectively, slightly lower than those observed at

276   Barrow. From 0:00 on March 14, σ_{sp}(PM$_1$) and σ_{sp}(PM$_{10}$) started to increase and

277   reached the maximum values of 18.6 Mm^{-1} and 32.3 Mm^{-1} at 0:00 on March 15, which

278   were more than 4 and 5 times of their annual average, respectively. The mean σ_{sp}(PM$_1$)/

279   σ_{sp}(PM$_{10}$) ratio during 11:00, March 14 to 7:00 on March 18 was 0.61 ± 0.03, also

280   indicating the enrichment of coarse particles. This episode is defined as CASE II.
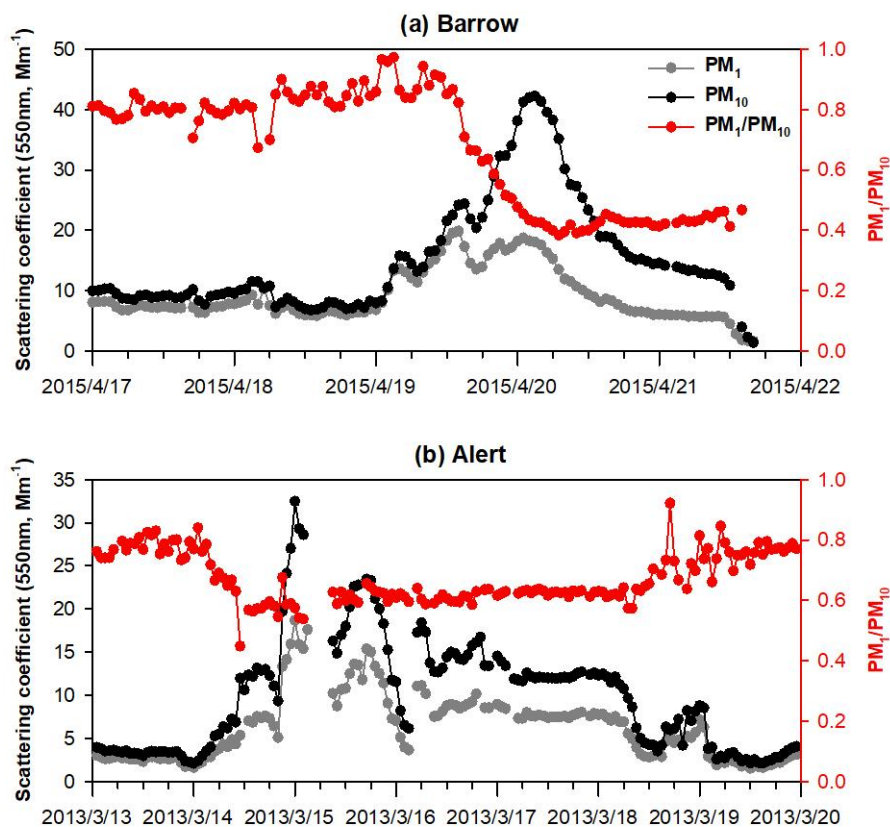
Figure 3. (a) Time series of hourly scattering coefficients of PM$_1$ and PM$_{10}$ at 550 nm and the ratio of PM$_1$/PM$_{10}$ at Barrow during April 17-21, 2015. (b) The same but for Alert during March 13 to 19, 2013.

In comparison, the pollution during CASE I lasted for a relatively short period of about 2.5 days while had higher peak values of $\sigma_{sp}(PM_{10})$ than CASE II, indicating that CASE I was subject to stronger long-range transport and more significant variations of synoptic conditions. The pollution during CASE II lasted for nearly four days, suggesting relatively weak cleanup processes of the air pollutants. As for the $\sigma_{sp}(PM_1)/\sigma_{sp}(PM_{10})$ ratio, it was much lower in CASE I than that in CASE II. This indicated the intrusion of coarse particles was more intense during CASE I, which could be related

293   to various factors such as the emission source regions, transport pathways, and

294   evolution of particles. In the next section, the transport pathways of the two cases above

295   were validated by using backward trajectory analysis and remote sensing from both

296   space and ground-based observations.

297

298   **3.4 Identification of dust long-range transport pathways**

299   To determine the sources and transport pathways of the two Arctic pollution events, the

300   HYSPLIT model was applied to compute the air masses transport trajectories. Figure

301   4a shows the 7-days backward trajectory simulated at an altitude of 6 km above Barrow

302   starting from 04:00 on April 20, 2015 (CASE I). The different segments of the trajectory

303   were colored to represent the continuous dates. On 14-15 April, air masses originated

304   from the Taklamakan and Gobi deserts in China, then passed over East Asia, Siberia of

305   Russia, and the Pacific Ocean, and finally reached Barrow about 6 days later. The

306   geopotential height fields based on the NCEP reanalysis data are plotted in Figure 4c-

307   4f to verify the dust transport path. On April 16, a low-pressure trough over Northeast

308   China caused the eastward air masses to turn northward. On April 17, the air masses

309   followed the high-pressure ridge over eastern Russia and entered the North Pacific.

310   Then its direction was again deflected by a low-pressure system near the Bering Strait

311   on April 18 and 19, finally reaching Barrow on April 20.
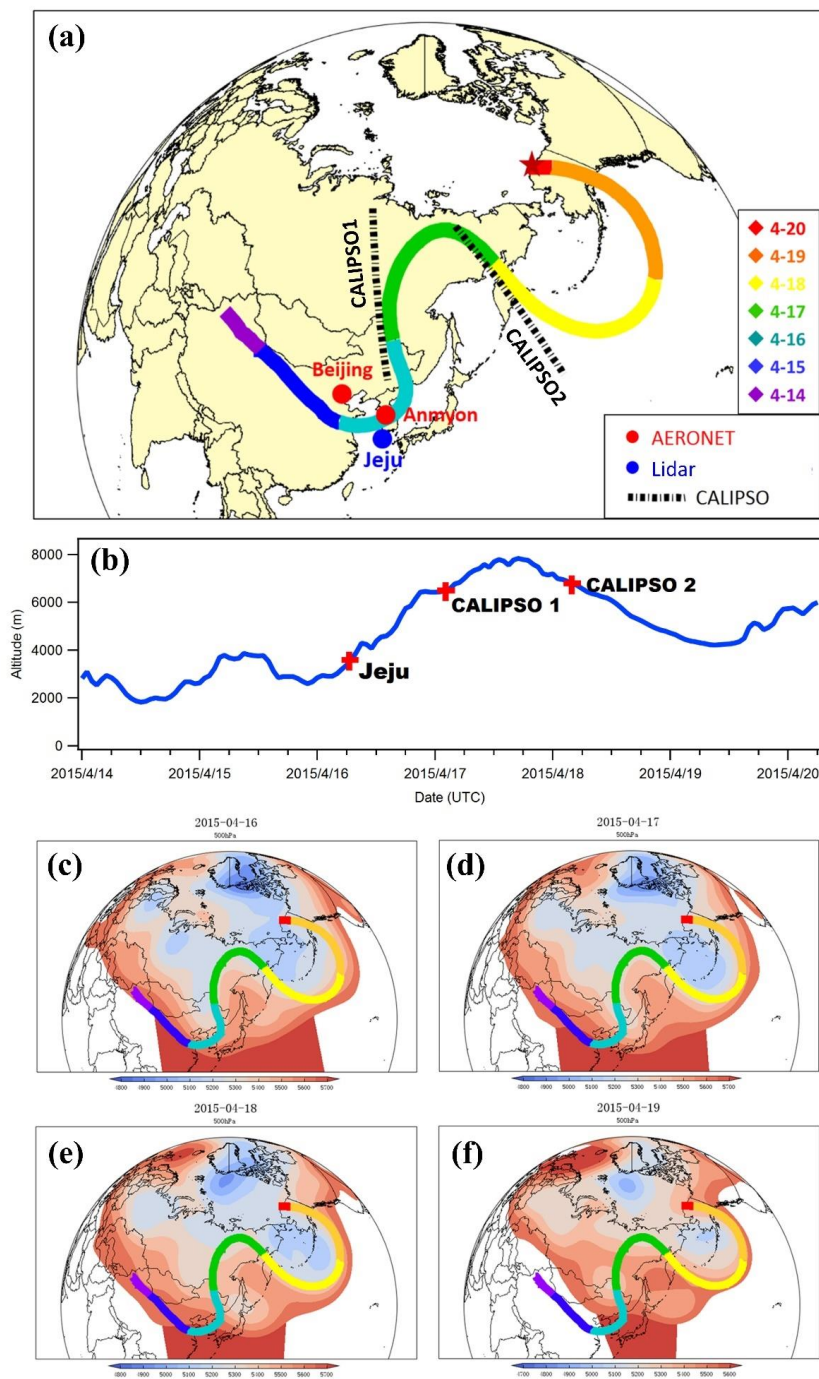
312
313
314 **Figure 4. (a) The 7-days backward trajectory simulated at an altitude of 6 km**

315 **above Barrow starting from 04:00 on April 20, 2015. The locations of AERONET,**
316 **Lidar sites, and CALIPSO tracks nearby the trajectory are plotted. (b) The height**
317 **of the trajectory along the transport path. The height and time of dust layers**
318 **observed by lidars and CALIPSO in Figure 4a are indicated by the red plus**
319 **symbols. (c-f) Daily geopotential height fields from the NCEP reanalysis data**

320

321 Figure 5a shows a typical backward trajectory simulated at an altitude of 4 km

322 above Alert on March 14, 2013 (CASE II). On March 7, air masses travelled over the

323 Gobi Desert on the border between Mongolia and the north of China, then passed over

324 Korea and Japan, and directly entered the Pacific Ocean. Afterwards, it kept moving

325 northward across the Arctic Ocean and reached Alert on March 14. Based on the

326 geopotential heights (Figure 5c-5h), a low-pressure system was observed over the

327 eastern coast of Russia and kept moving to the southeast from March 7 to 11. On March

328 11, the low-pressure system moved over the Sea of Okhotsk in Russia and turned to be

329 stronger, causing the air masses deflect and follow the geopotential height contours all

330 the way north to Alert.

331
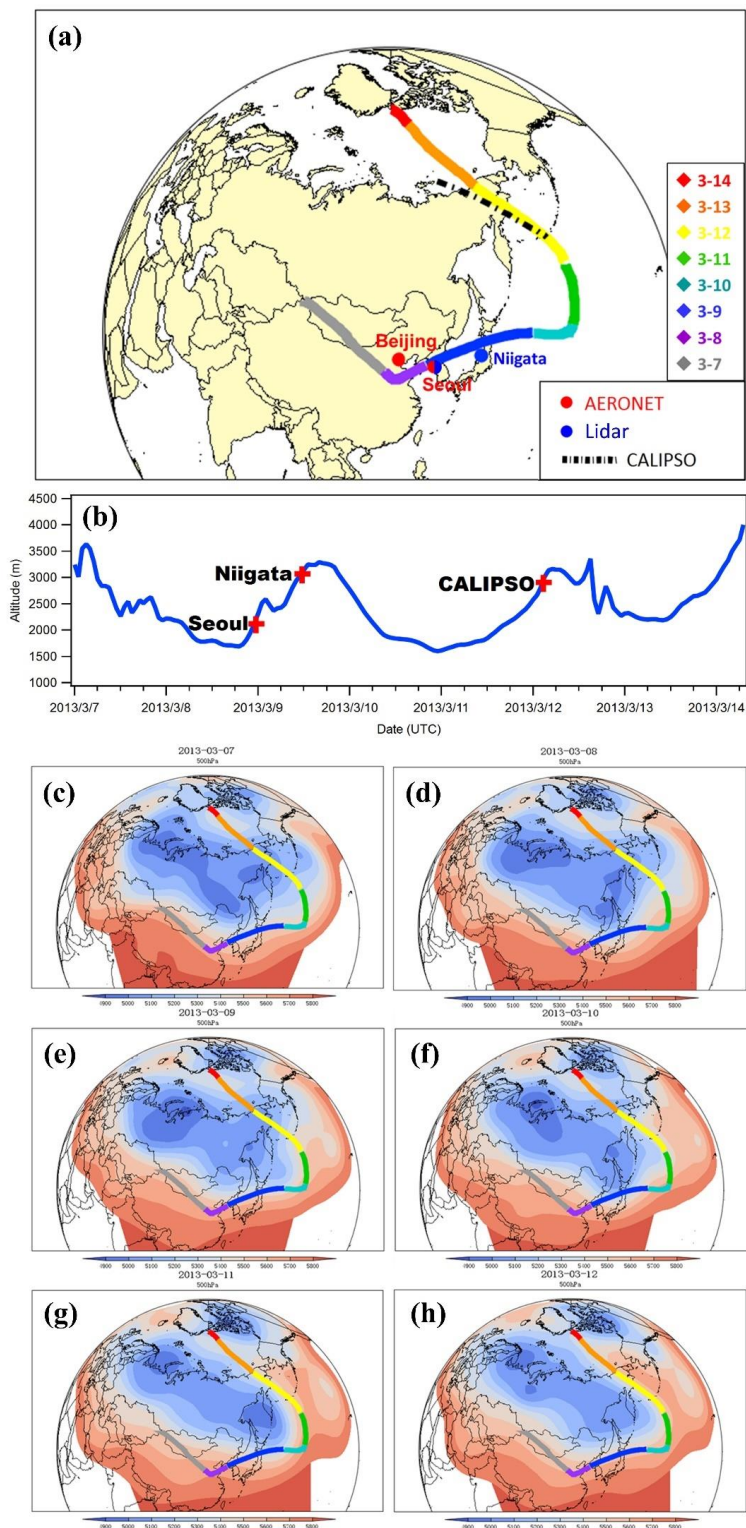
333 **Figure 5. Same as Figure 4 but for CASE II.**

334

335 **3.5 Verification of dust transport pathways based on satellite and ground-based**

336 **observations**

337 Although the air mass transport pathways of the two Arctic coarse particle pollution

338 cases were visualized based on trajectory modeling, whether dust particles were indeed

339 present in the air masses has not been confirmed. In this section, the aerosol optical

340 properties along the transport pathway were explored using both ground-based

341 observations (AERONET and AD-Net) and satellite inversion data (CALIPSO). In

342 Figure 4a and 5a, the red dots denoted the AERONET sites, which observed columnar

343 aerosol optical properties. The blue dots denoted the AD-Net sites, which observed

344 vertical profiles of aerosol extinctions and particle spheric information. The black

345 dashed lines represented the orbits of CALIPSO profiles, which were used to

346 supplement the aerosol information in the blank areas without available ground-based

347 observations. The validation results of the two cases are described separately as below.

348

349 **(i) CASE I**

350 Figures 6 shows the aerosol optical properties of two AERONET sites, i.e., Beijing

351 (China) and Anmyon (Korea), which were located nearby the air mass transport

352 pathway in CASE I (Figure 4a). AE (Angström exponent) is a parameter of

353 characterizing the particle size. The smaller AE represents the larger particle size, and

354 vice versa. In general, AE < 1 suggested the dominance of coarse particles, which were

355   usually associated with dust or sea salts. While AE > 1 suggested the dominance of fine

356   particles, which derived from anthropogenic emissions and biomass burning.

357   As shown in Figure 6a, AOD over Beijing doubled from about 1.0 at around 0:00

358   on April 15 to nearly 2.0 at around 6:00, while AE remained below 0.5. When the air

359   masses passed over Anmyon, Korea, AOD was about 0.4 at 8:00 on April 16 (Figure

360   6b). AOD at Anmyon was much lower compared to Beijing, which should be due to the

361   removal process during the transport and lower local emissions at Anmyon. Similarly,

362   AE at this site was low below 0.4 and it slightly increased to above 0.5 after 8:00. As a

363   whole, the observation of high AOD and low AE at both sites indicated that the air

364   masses contained abundant coarse dust aerosols.

365   Figure 6c shows the vertical profiles of aerosol optical properties over Jeju Island,

366   Korea. The depolarization ratio represents the degree of particle approximation to a

367   sphere in the range of 0 - 1. The depolarization ratio of a spherical object is equal to 0,

368   and vice versa (Mishra et al., 2010). Since dust aerosols were irregularly shaped

369   particles, the depolarization ratio of dust aerosols usually ranged between 0.2 and 0.3.

370   As for the intense dust storm events, the depolarization ratio of particles could reach

371   over 0.4 (Liu et al., 2003). High extinction coefficients and depolarization ratios

372   between 0.1 and 0.3 at around 4 km over Jeju in the early morning of April 16, 2015

373   were observed. By comparing the simulated height of the air mass backward trajectory

374   and the observed plume height over Jeju, good agreement was found (Figure 4b),

375   corroborating the same origin of the Arctic pollution and the Asian downstream dust

376   plumes.

377
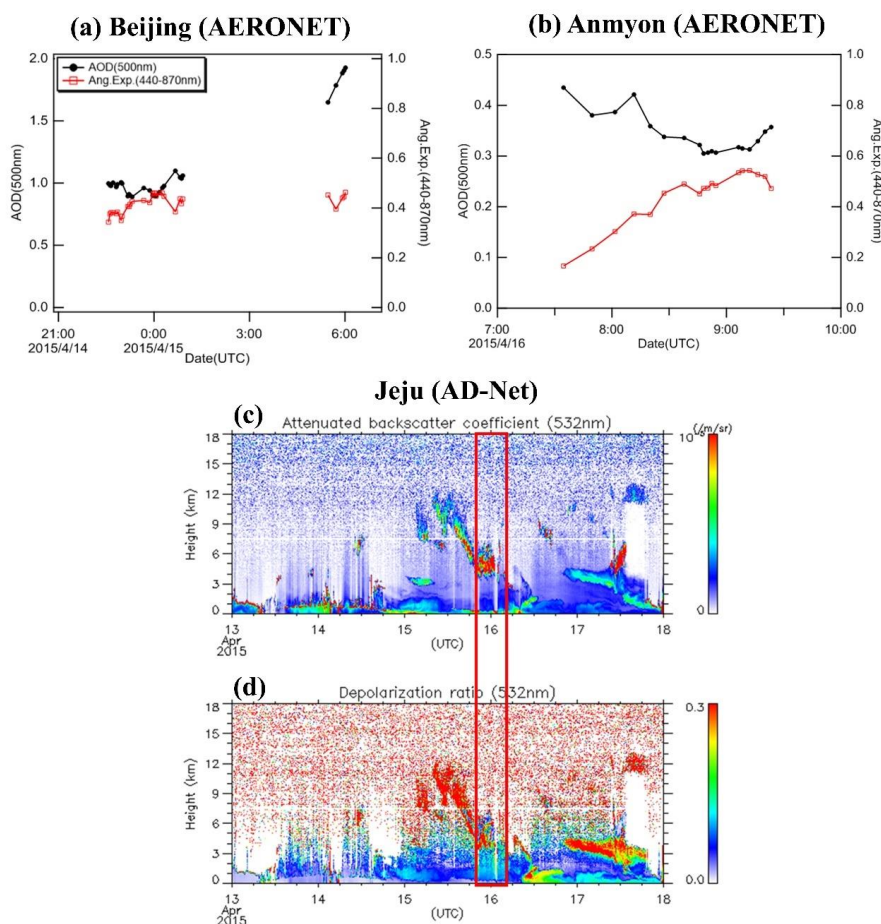
378
379 **Figure 6. Aerosol optical properties observed at ground-based sites during CASE**
380 **I. (a) AOD and Angström exponent at the Beijing AERONET site. (b) AOD and**
381 **Angström exponent at the Anmyon AERONET site. Vertical profiles of (c)**
382 **backscattering coefficient and (d) depolarization ratio at the Jeju AD-Net site. The**
383 **red rectangle denotes the time when dust passed over the site.**

384

385   After April 16, the dust plume moved towards Russia and the North Pacific. Due

386 to the lacking of ground-based observations in this region, CALIPSO inversion

387 products were used to fill in these blank regions. At about 5:00 UTC on April 17, 2015,

388 over the northeastern part of Russia (54.19°N, 122.17°E), CALIPSO observed an

389   aerosol layer, about 5 km above the ground. This height was generally consistent with

390   that of the simulated backward trajectory (Figure 4b) and the plume was identified as a

391   mixture of dust, polluted dust, and other types of aerosols (Figure 7). At 2:00 UTC on

392   April 18, CALIPSO observed a similar mixed layer of dust, polluting dust, and lifted

393   smoke at 4-6 km over the Kamchatka Peninsula in Russia (Figure 7). Compared to the

394   previous day, the lifted smoke was more abundant, suggesting that smoke aerosols from

395   forest fires may have been mixed with the air masses passed over Russia.
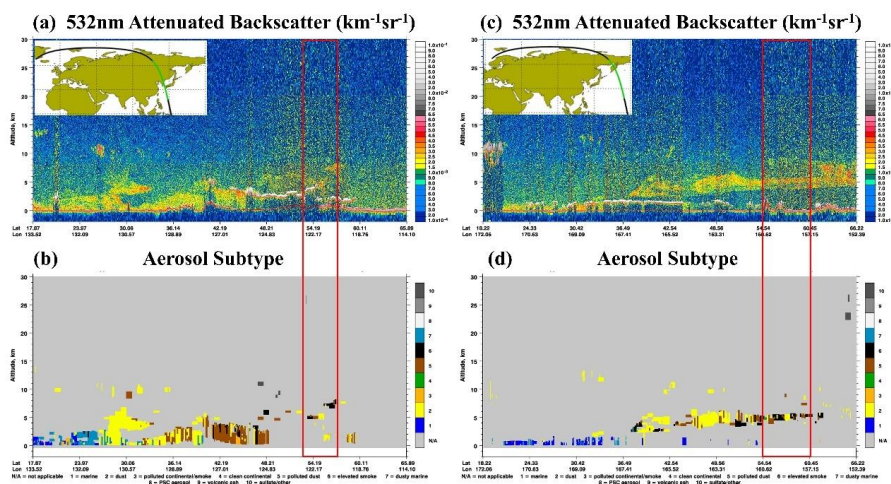
396
397
398   **Figure 7. CALIPSO profiles of aerosol backscattering coefficients and identified**
399   **aerosol types on April 17 (a-b) and 18 (c-d), 2015. The red rectangles denote the**
400   **regions as indicated by the CALIPSO tracks in Figure 4a.**
401

402   **(ii) CASE II**

403   Figure 8 shows the available ground-based observations close to the transport pathway

404   during CASE II. At the Beijing AERONET site, at 3:00 UTC on March 8, 2013, AOD

405   was 0.73 while AE was 0.47. This was indicative of the dominance of dust particles.

406   Afterwards at 8:00, AOD increased more than twice and approached 2.5, while AE also

407   increased to more than 0.9, indicating that the dust in CASE II was more mixed with

408   fine particles than CASE I.

409   From 0:00 to 6:00 UTC on March 9, 2013, observed AE at the Seoul AERONET

410   site decreased to a low level of about 0.6 and increased to around 1.0 for several hours.

411   This process was accompanied by a continuous increase of AOD, reaching a maximum

412   of 1.15. In addition, the vertical profiles of the aerosol optical properties in the early

413   morning of March 9 indicated a 1-2 km thick dust layer at altitudes of 1-3 km height

414   over Seoul (Figure 8c), which was in good agreement with the height of the backward

415   trajectory (Figure 5b). Figure 8d shows the lidar vertical observations in Niigata, Japan.

416   A 1-2km thick dust layer at altitudes of 2 – 4km was also observed at 9:00-12:00 UTC

417   on March 9. The heights of the dust layers observed from lidars were also in good

418   agreement with the time and height of the simulated backward trajectory as shown in

419   Figure 5b.

420
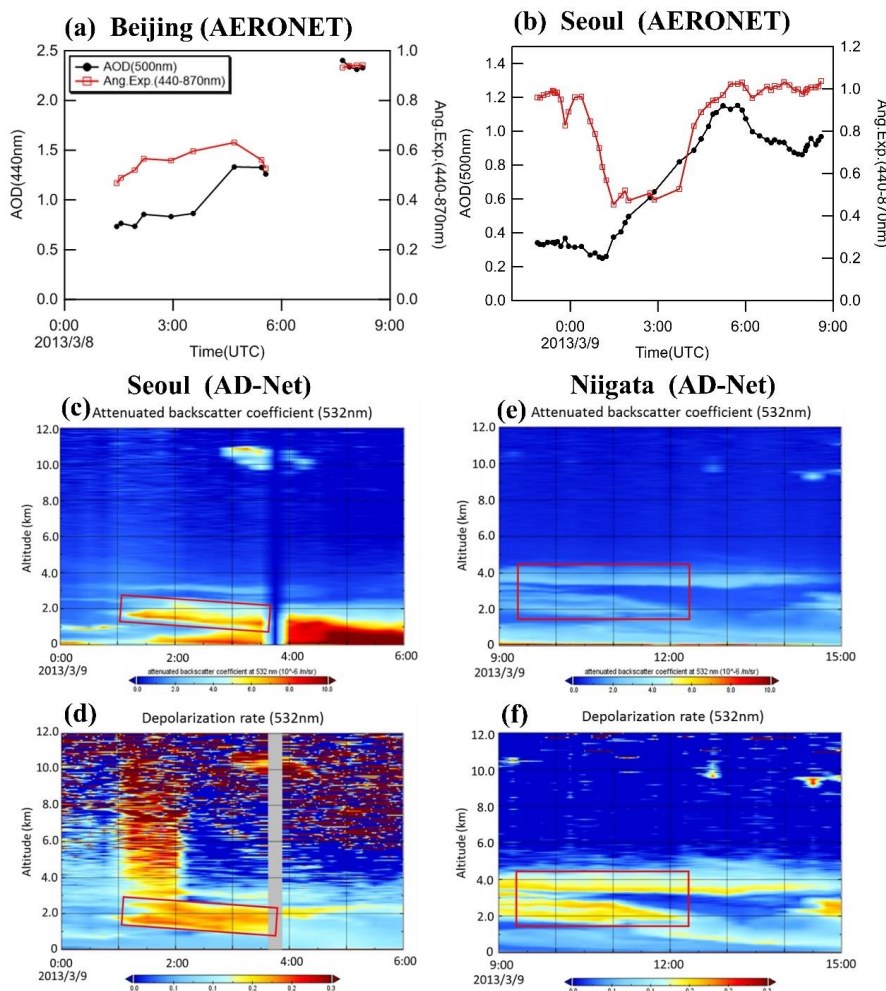
Figure 8. Aerosol optical properties observed at ground-based sites during CASE II. (a) AOD and Angström exponent at the Beijing AERONET site (b) AOD and Angström exponent at the Seoul AERONET site (c-d) Vertical profiles of backscattering coefficient and depolarization ratio at the Seoul AD-Net site (e-f) Vertical profiles of backscattering coefficient and depolarization ratio at the Niigata AD-Net site. The red rectangle denotes the time when dust passed over the site.

Figure 9 shows the aerosol vertical structure observed from CALIPSO over the

Bering Sea (51.28°N, 175.96°E - 57.23°N, 172.96°E) on March 12, 2013. At around

2.5 - 4 km, an aerosol layer was evident, consisting of dust and polluted dust,

433   confirming that the aerosols transported to the remote ocean still contained a large

434   amount of dust particles.

(a) 532nm Attenuated Backscatter (km⁻¹sr⁻¹)

(b)   Aerosol Subtype

435

436
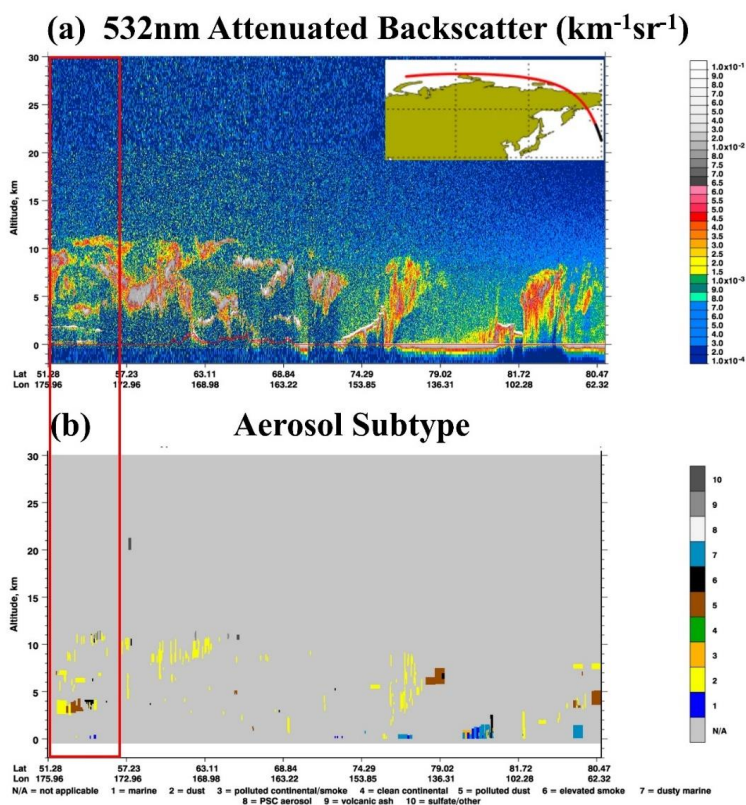
Figure 9. CALIPSO profiles of (a) aerosol backscattering coefficients and (b)
identified aerosol types on March 12, 2013. The red rectangles denote the regions
as indicated by the CALIPSO tracks in Figure 5a.

440

441   By comparing the transport pathways of CASE I and CASE II, CASE I passed

442   over more terrestrial areas, increasing the probability of mixing between dust and air

443   pollutants from anthropogenic emissions. While CASE II travelled more over the open

444   ocean, which was more likely to mix with sea salts. In terms of transport time, the air

445   masses in CASE I took about four days to reach the receptor after getting out of the

446 Asian dust source regions, while the air masses in CASE II took about six days. The

447 longer transport time in CASE II may lead to more deposition of coarse dust particles

448 due to the gravitational effect and other removing processes such as wet scavenging.

449

450 **3.6 Evolution of aerosol optical properties during long-range transport to the**

451 **Arctic**

452 In the previous section, it has been well demonstrated that the Arctic air pollution events

453 in both CASE I and CASE II were caused by the long-range transport of Asian dust.

454 However, only a limited observation from ground-based sites and CALIPSO was

455 available for the analysis of aerosol properties. In order to analyze the evolution of

456 aerosols during the transport, MODIS data with a wide spatial coverage was used to

457 quantify the changes of aerosol optical properties.

458 As shown in Figure S1, MODIS data were analyzed on a daily basis. Since

459 simulated backward trajectories were subject to certain uncertainties (Draxler and Hess,

460 1998), the rectangular subsection that covered the daily trajectory was extracted to

461 represent the aerosol properties along the transport pathway. Figure 10 compares the

462 mean values of AOD and AE over the daily transport coverage area between the two

463 cases. As shown in Figure 10a, AOD in CASE I exhibited an evidently decreasing trend

464 with time. It averaged 0.86 on April 14, 2015 over the dust source regions, while it was

465 0.10 at Barrow on April 20, indicating a tremendous AOD decrease of nearly 8 times.

466 In the meanwhile, AE showed an increasing trend (Figure 10b). This indicated that, on

467 the one hand, the high aerosol concentrations from the dust source regions had been

468 significantly eliminated by various physical scavenging processes. On the other hand,

469 dust mixed with fine particles such as black carbon, nitrate, and sulfate and gradually

470 modified the irregular dust particles to be more spheric.

471   In contrast, less variation of AOD during the transport was observed in CASE II

472 (Figure 10c). The level of AOD stayed in the range of 0.56 - 0.68 from March 8 to 11.

473 Meanwhile, except for the low value of AE on March 8 (possibly due to the small

474 number of data points as shown in Figure S1b), the mean AE values were above 1.0 on

475 March 7 and 9. This suggested that dust mixed with more fine particles and coarse

476 particles were more removed. Overall, by comparing these two cases, it was evident

477 that different transport routes to the Arctic had divergent effects on the evolution of

478 aerosol optical properties.

479
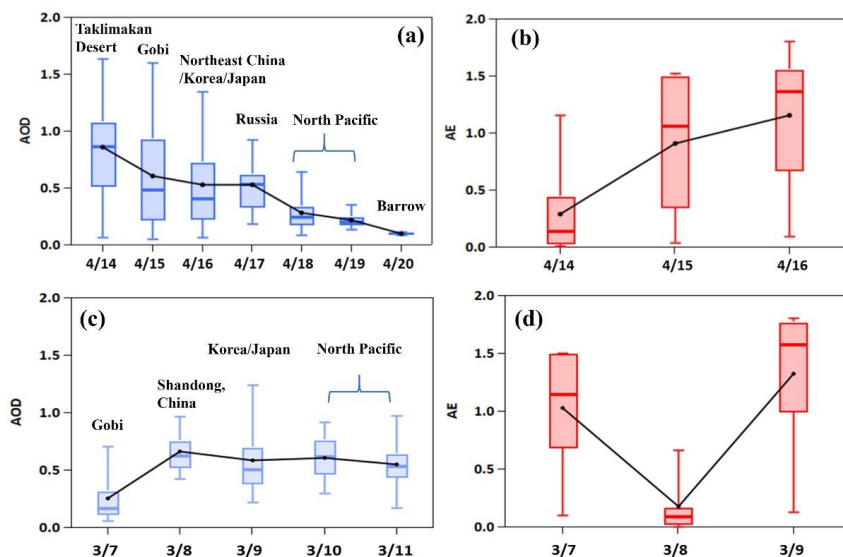
480
481
482 **Figure 10. Regional (a) AOD and (b) Angström exponent in CASE I. Regional (c)**
483 **AOD and (d) Angström exponent in CASE II. The dots and lines inside the boxes**

484 **represent the mean and median values, respectively; bottom and top of the boxes**
485 **represent the 25 and 75% limits, respectively; and bottom and top short lines**
486 **represent the minimum and maximum values, respectively. The geographic region**
487 **in each day is defined in Figure S1.**

488

489 **3.7 Impact assessment of transported aerosols on the Arctic surface albedo**

490 Surface albedo is an important parameter for energy exchange between the surface and

491 the atmosphere in polar regions. The changes in snow and ice albedos could have

492 important climatic impacts on the polar regions as well as the whole world. Due to the

493 large difference between the multiple scattering effect of snow and ice and absorption

494 effects of absorbing impurities (e.g. black carbon and dust), very small amounts of

495 deposited impurities can lead to a decrease of snow and ice albedo (Zhang et al., 2017).

496 Hansen and Nazarenko (2004) showed that the effect of soot on reducing snow and ice

497 albedo was around 1.5% in the Arctic and 3% in the snow and ice covered areas of the

498 Northern Hemisphere. Kaspari et al. (2014) showed that black carbon reduced snow

499 and ice albedo by 6-10% relative to pure snow in the Himalayas in winter and spring,

500 and other impurities such as dust even reduced snow and ice albedo by 40 - 42%. In

501 this regard, decreases of snow and ice albedo would cause surface warming, thinning

502 of sea ice, melting permafrost, and consequently sea level rise that may have serious

503 impacts on the global water resources and ecosystems.

504 In this section, the impacts of the two Arctic pollution events on changing the surface

505 albedo were assessed. The SNICAR snow and ice albedo model was applied to estimate

506 the contributions of dust and black carbon to the reduction of snow and ice albedo.

507

3.7.1 Estimation of mass concentrations of impurities in snow and evaluation of

model performance

In this study, we only considered airborne dust and elemental carbon (EC) as the

dominant contributors to the impurities in the Arctic snow and ice. Firstly, the

atmospheric concentrations of absorbing aerosols were estimated by using the revised

IMPROVE (The Interagency Monitoring of Protected Visual Environments) Equation

(Pitchford et al., 2007). It was assumed that airborne dust and EC dominated the

scattering of coarse particles and absorption of fine particles, respectively (Eq. 1-2).

$C_{dust} = b_{sca,(PM10-PM1)} / 0.6$,   (1)

$C_{EC} = b_{abs,PM1} / 10$,   (2)

Of which, the constant 0.6 and 10 (m^2/g) is the mass scattering efficiency and mass

absorption efficiency of dust and EC, respectively (Pitchford et al., 2007). Since the

concentrations of impurities in snow were required as inputs for the SNICAR model,

we estimated them based on the following assumption. Dou et al. (2017) conducted

field sampling at Barrow during April and May in 2015 and measured elemental carbon

concentration of 3.30 ng/g in the snow sample on April 30, 2015. The airborne

elemental carbon concentration was estimated to be 6.25 ng/m^3 on the same day by

using the equations above. Thus, the ratio of the particulate matter in the snow versus

that in the atmosphere was calculated to be 0.528m^3/g. This ratio was then applied to

estimate the concentrations of dust and elemental carbon in snow during the two cases.

To evaluate the model performance, Figure S2 compares the simulated values of

surface albedo and the observations at an ARM (Atmospheric Radiation Measurement)

530   site located at Barrow during 14 – 19, April, 2015. A correlation coefficient of 0.74 was

531   derived, indicating the relatively good model performance on simulating the Arctic

532   surface albedo. However, deviations of simulated values from observations were still

533   found. The bias may derive from the following aspects. First, the concentrations of dust

534   and elemental carbon in snow as inputs for the model were not in-situ measured, as well

535   as for the other input parameters such as snow radius, thickness, and density. Secondly,

536   the simulation only considered the absorbing substances deposited from the atmosphere

537   while the pre-existing impurities in snow and ice were ignored. Last but not the least,

538   impurities such as brown carbon were not included for the simulation.

539

540   **3.7.2 Comparison of the changes of Arctic surface albedo between two cases**

541   In this section, the impacts of transported particles on the change of surface albedo in

542   both cases were evaluated. Figure S3 shows the time-series of estimated dust and

543   elemental carbon in snow during the two pollution cases. As for CASE I (Figure S3a),

544   the peak time of elemental carbon was about half a day ahead of that of dust. This

545   phenomenon was as similar as some other dust events that anthropogenic air pollutants

546   were ahead of dust pushed by the cold front (Guo et al., 2004; Wang et al., 2018a). In

547   regard of the variations of pollutants, four representative moments were selected, i.e.,

548   0:00 on April 18 (the beginning of pollution), 13:00 on April 19 (the peak time of

549   elemental carbon), 3:00 on April 20 (the peak time of dust), and 15:00 on April 21 (the

550   end of pollution). As for CASE II (Figure S3b), the estimated concentrations of

551   impurities in snow stayed at relatively low levels and varied less strongly compared to

552   CASE I. We chose 12:00 on March 14 (the beginning of pollution), 17:00 on March 15

553   (the peak time of dust), and 13:00 on March 18 (the end of pollution) for the analysis.

554   By using the SNICAR model, the effects of dust, elemental carbon, and

555   combination of dust and elemental carbon on the surface albedo were separately

556   assessed. As shown in Table 4, the reduction of surface albedo caused by long-range

557   transported Asian light-absorbing pollutants ranged from 0.35% to 2.63%, which were

558   consistent with previous studies. For instance, Dou et al. (2017) calculated a 1.6-5.1%

559   reduction in snow and ice albedo caused by dust and black carbon at Barrow from late

560   April to May 2015, with a 5-10 fold increase in pollutant concentrations compared to

561   the pre-April period due to the snowmelt period during that time. Zhang et al. (2017)

562   calculated that dust and black carbon reduced snow and ice albedo by 0.72-1.00% on

563   glaciers in the southeastern Tibetan Plateau in June 2015. In CASE I, the highest

564   concentration of elemental carbon in snow reached more than 72 ng/g, which could

565   reduce the albedo by 1.47%. And the highest concentration of dust reached more than

566   37 μg/g, which could reduce the albedo by 2.26%. During this pollution event, the

567   combined effect of dust and elemental carbon significantly reduced the snow and ice

568   albedo by 2.28%. In CASE II, elemental carbon concentrations were much lower than

569   CASE I and its effect on albedo was below 0.40%, while dust can reduce albedo up to

570   1.87%. The combined effect of dust and elemental carbon reached more than 2%

571   compared to the pure snow condition.

572

573   **Table 4. Simulated changes of albedo due to dust, elemental carbon, and**

574   **combination of dust and elemental carbon (SA represents the simulated surface**

575 **albedo of pure snow)**

Time (UTC)	BC snow (ng/g)	Dust snow (μg/g)	SA Pure	SA+EC	SA+Dust	SA+EC & Dust	EC (%)	Dust (%)	EC&Dust (%)
Barrow									
2015/4/18 0:00	24.31	8.31	0.7990	0.7901	0.7915	0.7852	1.12%	0.94%	1.73%
2015/4/15 15:00	72.14	21.39	0.8392	0.8270	0.8300	0.8218	1.47%	1.10%	2.07%
2015/4/20 3:00	21.16	37.11	0.8143	0.8077	0.7959	0.7929	0.83%	2.26%	2.63%
2015/4/21 15:00	6.08	1.93	0.8379	0.8361	0.8365	0.8350	0.22%	0.17%	0.35%
Alert									
2013/3/14 13:00	7.75	10.77	0.7995	0.7964	0.7912	0.7891	0.39%	1.04%	1.30%
2013/3/15 17:00	7.37	20.74	0.7923	0.7892	0.7775	0.7758	0.40%	1.87%	2.08%
2013/3/18 13:00	6.52	3.68	0.7956	0.7929	0.7921	0.7899	0.34%	0.44%	0.72%

576

577   As discussed above, the concentrations of dust and elemental carbon were

578   relatively higher in CASE I, hence the resulting effects on snow and ice albedo were

579   more obvious. On the one hand, the transport time in CASE I was shorter and the

580   particulate matters were scavenged less along the transport. On the other hand, the air

581   masses in CASE I passed over a large number of terrestrial areas, including northeast

582   China and Siberia. Fine particles from anthropogenic emissions and biomass burning

583   in Siberia mixed with dust and transported to Barrow together, making the elemental

584   carbon at the receptor significantly higher. As for CASE II, the receptor site at Alert is

585   a higher latitudinal area, which was much less affected by local anthropogenic activities.

586 In addition, the transport pathway of CASE II was mostly over the open ocean with

587 longer duration. This finally induced much lower air pollutant concentrations and

588 weaker impact on the reduction of surface albedo.

589

4. Conclusions

591 In this study, the long-range transport of Asian dust to the Arctic was investigated.

592 During 2011-2015, 50 dust events in China were recorded, of which 38 dust events had

593 the capability to reach the Arctic based on the air mass trajectory simulation. Two main

594 transport routes were identified. One typical transport type was characterized of wide

595 geographic coverage, long transport duration (generally 7-10 days), and mainly marine

596 transport due to the high lifting altitude of dust particles (mostly over 1500m) over the

597 dust source regions. The other typical transport type was characterized of dust transport

598 mostly over land with relatively short duration of about 4-8 days. This was due to the

599 presence of a low-pressure system over northern Japan in spring, which induced the air

600 masses deflecting northward.

601 Two typical coarse particle dominated cases observed in the Arctic were

602 specifically investigated, i.e., one at Barrow in April 2015 (CASE I) and the other one

603 at Alert in March 2013 (CASE II), respectively. Based on the air mass trajectory

604 simulation, in CASE I, dust originated from the Taklamakan and Gobi deserts in China,

605 then passed over East Asia, Siberia of Russia, and the Pacific Ocean, and finally reached

606 Barrow. In CASE II, dust originated from the Gobi Desert, then passed over Korea and

607 Japan and directly entered the Pacific Ocean, and finally moved northward across the

608   Arctic Ocean and reached Alert.

609   The dust transport pathways during both cases were verified based on a synergy

610   of NCEP reanalysis data (geopotential height fields), ground-based observations

611   (AERONET aerosol columnar properties and lidar aerosol profiles), and satellite

612   products (CALIPSO profiles). The passing time and height of the dust plume based on

613   trajectory simulation coincided very consistently with various observations. The

614   evolution of aerosol optical properties during the transport was assessed by using the

615   large-scale MODIS data. In CASE I, AOD showed a significant decreasing trend while

616   Angström exponent showed an increasing trend from the dust source region to the

617   receptor. In contrast, AOD varied much less significantly in CASE II. It was evident

618   that different transport routes to the Arctic had divergent effects on the evolution of

619   aerosol properties.

620   The SNICAR snow and ice model was applied to simulate the impact of impurities

621   on the reduction of surface albedo in the Arctic during the two cases. The concentrations

622   of dust and elemental carbon in snow were estimated and the effects of dust, elemental

623   carbon, and combination of dust and elemental carbon on snow and ice albedo were

624   separately quantified. The reduction of snow and ice albedo caused by long-range

625   transported Asian light-absorbing pollutants ranged from 0.35% to 2.63%. This study

626   highlighted that the long-range transport of Asian dust to the Arctic was ubiquitous and

627   its impact on changing the radiative forcing and regional climate in the Arctic should

628   be considered by the atmosphere-ocean-cryosphere interaction.

629

Data availability

The measurement data at Barrow and Alert are from the EBAS database

(https://ebas.nilu.no/). Aerosol columnar data are from AERONET

(https://aeronet.gsfc.nasa.gov/). Aerosol vertical profiles are from AD-Net

(https://www-lidar.nies.go.jp/AD-Net). The MODIS Level-3 aerosol products are

from NASA's Giovanni (https://giovanni. gsfc.nasa.gov/giovanni/). The NCEP/NCAR

reanalysis data are from https://www.esrl.noaa.gov/psd/data/gridded/reanalysis/

Author contributions

KH designed this study. XZ analyzed data. All reviewed and wrote the paper.

Competing interests

The authors declare that they have no conflict of interest.

Acknowledgements

We sincerely thank for EBAS, AERONET, AD-Net, NASA, and NCEP/NCAR for

providing the observational and modeling data. This work was supported by the

National Natural Science Foundation of China (42175119, 91644105) and the National

Natural Science Foundation of Shanghai (18230722600). Kan Huang also

acknowledges Jiangsu Shuangchuang Program through Jiangsu Fuyu Environmental

Technology Co., Ltd.

References:

Blanchet, J. P. and List, R.: Estimation of optical properties of arctic haze using a numerical model, Atmosphere-Ocean, 21, 444-465, 10.1080/07055900.1983.9649179, 2010.

Breider, T. J., Mickley, L. J., Jacob, D. J., Ge, C., Wang, J., Sulprizio, M. P., Croft, B., Ridley, D. A., McConnell, J. R., Sharma, S., Husain, L., Dutkiewicz, V. A., Eleftheriadis, K., Skov, H., and Hopke, P. K.: Multidecadal trends in aerosol radiative forcing over the Arctic: Contribution of changes in anthropogenic aerosol to Arctic warming since 1980, Journal of Geophysical Research-Atmospheres, 122, 3573-3594, 10.1002/2016jd025321, 2017.

Brock, C. A., Cozic, J., Bahreini, R., Froyd, K. D., Middlebrook, A. M., McComiskey, A., Brioude, J., Cooper, O. R., Stohl, A., Aikin, K. C., de Gouw, J. A., Fahey, D. W., Ferrare, R. A., Gao, R. S., Gore, W., Holloway, J. S., Huebler, G., Jefferson, A., Lack, D. A., Lance, S., Moore, R. H., Murphy, D. M., Nenes, A., Novelli, P. C., Nowak, J. B., Ogren, J. A., Peischl, J., Pierce, R. B., Pilewskie, P., Quinn, P. K., Ryerson, T. B., Schmidt, K. S., Schwarz, J. P., Sodemann, H., Spackman, J. R., Stark, H., Thomson, D. S., Thornberry, T., Veres, P., Watts, L. A., Warneke, C., and Wollny, A. G.: Characteristics, sources, and transport of aerosols measured in spring 2008 during the aerosol, radiation, and cloud processes affecting Arctic Climate (ARCPAC) Project, Atmospheric Chemistry and Physics, 11, 2423-2453, 10.5194/acp-11-2423-2011, 2011.

CMA: (China Meteorological Administration Eds.): Sand-dust Weather Almanac (2011), China Meteorological Press, Beijing, China, 2013.

CMA: (China Meteorological Administration Eds.): Sand-dust Weather Almanac (2012), China Meteorological Press, Beijing, China, 2014.

CMA: (China Meteorological Administration Eds.): Sand-dust Weather Almanac (2013), China Meteorological Press, Beijing, China, 2015.

CMA: (China Meteorological Administration Eds.): Sand-dust Weather Almanac (2014), China Meteorological Press, Beijing, China, 2016.

CMA: (China Meteorological Administration Eds.): Sand-dust Weather Almanac (2015), China Meteorological Press, Beijing, China, 2017.

Dagsson-Waldhauserova, P., Renard, J. B., Olafsson, H., Vignelles, D., Berthet, G., Verdier, N., and Duverger, V.: Vertical distribution of aerosols in dust storms during the Arctic winter, Sci Rep-Uk, 9, 2019.

Di Biagio, C., Pelon, J., Ancellet, G., Bazureau, A., and Mariage, V.: Sources, Load, Vertical Distribution, and Fate of Wintertime Aerosols North of Svalbard From Combined V4 CALIOP Data, Ground-Based IAOOS Lidar Observations and Trajectory Analysis, Journal of Geophysical Research-Atmospheres, 123, 1363-1383, 10.1002/2017jd027530, 2018.

Di Pierro, M., Jaegle, L., and Anderson, T. L.: Satellite observations of aerosol transport from East Asia to the Arctic: three case studies, Atmospheric Chemistry and Physics, 11, 2225-2243, 10.5194/acp-11-2225-2011, 2011.

Domine, F., Cabanes, A., and Legagneux, L.: Structure, microphysics, and surface area of the Arctic snowpack near Alert during the ALERT 2000 campaign, Atmospheric Environment, 36, 2753-2765, 10.1016/s1352-2310(02)00108-5, 2002.

Dong, X., Xi, B., Crosby, K., Long, C. N., Stone, R. S., and Shupe, M. D.: A 10 year climatology of Arctic cloud fraction and radiative forcing at Barrow, Alaska, Journal of Geophysical Research-Atmospheres, 115, 10.1029/2009jd013489, 2010.

695   Dou, T., Xiao, C., Du, Z., Schauer, J. J., Ren, H., Ge, B., Xie, A., Tan, J., Fu, P., and Zhang, Y.: Sources,
696   evolution and impacts of EC and OC in snow on sea ice: a measurement study in Barrow, Alaska, Science
697   Bulletin, 62, 1547-1554, 10.1016/j.scib.2017.10.014, 2017.
698   Draxier, R. R. and Hess, G. D.: An overview of the HYSPLIT_4 modelling system for trajectories,
699   dispersion and deposition, Aust Meteorol Mag, 47, 295-308, 1998.
700   Fan, S. M.: Modeling of observed mineral dust aerosols in the arctic and the impact on winter season
701   low-level clouds, J Geophys Res-Atmos, 118, 11161-11174, 2013.
702   Ferrero, L., Ritter, C., Cappelletti, D., Moroni, B., Mocnik, G., Mazzola, M., Lupi, A., Becagli, S.,
703   Traversi, R., Cataldi, M., Neuber, R., Vitale, V., and Bolzacchini, E.: Aerosol optical properties in the
704   Arctic: The role of aerosol chemistry and dust composition in a closure experiment between Lidar and
705   tethered balloon vertical profiles, Sci Total Environ, 686, 452-467, 2019.
706   Fisher, J. A., Jacob, D. J., Wang, Q., Bahreini, R., Carouge, C. C., Cubison, M. J., Dibb, J. E., Diehl, T.,
707   Jimenez, J. L., Leibensperger, E. M., Lu, Z., Meinders, M. B. J., Pye, H. O. T., Quinn, P. K., Sharma, S.,
708   Streets, D. G., van Donkelaar, A., and Yantosca, R. M.: Sources, distribution, and acidity of sulfate-
709   ammonium aerosol in the Arctic in winter-spring, Atmospheric Environment, 45, 7301-7318,
710   10.1016/j.atmosenv.2011.08.030, 2011.
711   Flanner, M. G.: Arctic climate sensitivity to local black carbon, Journal of Geophysical Research-
712   Atmospheres, 118, 1840-1851, 10.1002/jgrd.50176, 2013.
713   Flanner, M. G., Zender, C. S., Randerson, J. T., and Rasch, P. J.: Present-day climate forcing and response
714   from black carbon in snow, Journal of Geophysical Research-Atmospheres, 112, 10.1029/2006jd008003,
715   2007.
716   Gagne, M.-E., Fyfe, J. C., Gillett, N. P., Polyakov, I. V., and Flato, G. M.: Aerosol-driven increase in
717   Arctic sea ice over the middle of the twentieth century, Geophysical Research Letters, 44, 7338-7346,
718   10.1002/2016gl071941, 2017.
719   Gillett, N. P., Stone, D. A., Stott, P. A., Nozawa, T., Karpechko, A. Y., Hegerl, G. C., Wehner, M. F., and
720   Jones, P. D.: Attribution of polar warming to human influence, Nature Geoscience, 1, 750-754,
721   10.1038/ngeo338, 2008.
722   Ginoux, P., Prospero, J. M., Gill, T. E., Hsu, N. C., and Zhao, M.: Global-Scale Attribution of
723   Anthropogenic and Natural Dust Sources and Their Emission Rates Based on Modis Deep Blue Aerosol
724   Products, Rev Geophys, 50, 2012.
725   Guo, J., Rahn, K. A., and Zhuang, G. S.: A mechanism for the increase of pollution elements in dust
726   storms in Beijing, Atmos. Environ., 38, 855–862, 2004.
727   Guo, J., Lou, M., Miao, Y., Wang, Y., Zeng, Z., Liu, H., He, J., Xu, H., Wang, F., Min, M., and Zhai, P.:
728   Trans-Pacific transport of dust aerosols from East Asia: Insights gained from multiple observations and
729   modeling, Environmental Pollution, 230, 1030-1039, 10.1016/j.envpol.2017.07.062, 2017.
730   Hansen, J. and Nazarenko, L.: Soot climate forcing via snow and ice albedos, Proceedings of the National
731   Academy of Sciences of the United States of America, 101, 423-428, 10.1073/pnas.2237157100, 2004.
732   Holben, B. N., Eck, T. F., Slutsker, I., Tanre, D., Buis, J. P., Setzer, A., Vermote, E., Reagan, J. A.,
733   Kaufman, Y. J., Nakajima, T., Lavenu, F., Jankowiak, I., and Smirnov, A.: AERONET - A federated
734   instrument network and data archive for aerosol characterization, Remote Sens Environ, 66, 1-16, Doi
735   10.1016/S0034-4257(98)00031-5, 1998.
736   Huang, Z., Huang, J., Hayasaka, T., Wang, S., Zhou, T., and Jin, H.: Short-cut transport path for Asian
737   dust directly to the Arctic: a case study, Environmental Research Letters, 10, 10.1088/1748-
738   9326/10/11/114018, 2015a.

739 Huang, Z. W., Huang, J. P., Hayasaka, T., Wang, S. S., Zhou, T., and Jin, H. C.: Short-cut transport path
740 for Asian dust directly to the Arctic: a case study, Environ Res Lett, 10, 2015b.

741 Kaspari, S., Painter, T. H., Gysel, M., Skiles, S. M., and Schwikowski, M.: Seasonal and elevational
742 variations of black carbon and dust in snow and ice in the Solu-Khumbu, Nepal and estimated radiative
743 forcings, Atmospheric Chemistry and Physics, 14, 8089-8103, 10.5194/acp-14-8089-2014, 2014.

744 Koch, D. and Del Genio, A. D.: Black carbon semi-direct effects on cloud cover: review and synthesis,
745 Atmospheric Chemistry and Physics, 10, 7685-7696, 10.5194/acp-10-7685-2010, 2010.

746 Kylling, A., Zwaaftink, C. D. G., and Stohl, A.: Mineral Dust Instantaneous Radiative Forcing in the
747 Arctic, Geophys Res Lett, 45, 4290-4298, 2018.

748 Liu, D., Qi, F. D., Jin, C. J., Yue, G. M., and ZHou, J.: Polarization lidar observations of cirrus clouds
749 and Asian dust aerosols over Hefei, Chinese Journal of Atmospheric Sciences, 27, 1093 - 1100, 2003.

750 Liu, H., Liu, X. D., and Dong, B. W.: Influence of Central Siberian Snow-Albedo Feedback on the Spring
751 East Asian Dust Cycle and Connection With the Preceding Winter Arctic Oscillation, J Geophys Res-
752 Atmos, 123, 13368-13385, 2018.

753 Marelle, L., Raut, J. C., Thomas, J. L., Law, K. S., Quennehen, B., Ancellet, G., Pelon, J.,
754 Schwarzenboeck, A., and Fast, J. D.: Transport of anthropogenic and biomass burning aerosols from
755 Europe to the Arctic during spring 2008, Atmospheric Chemistry and Physics, 15, 3831-3850,
756 10.5194/acp-15-3831-2015, 2015.

757 Mishra, M. K., Rajeev, K., Thampi, B. V., Parameswaran, K., and Nair, A. K. M.: Micro pulse lidar
758 observations of mineral dust layer in the lower troposphere over the southwest coast of Peninsular India
759 during the Asian summer monsoon season, Journal of Atmospheric and Solar-Terrestrial Physics, 72,
760 1251-1259, 10.1016/j.jastp.2010.08.012, 2010.

761 Pitchford, M., Malm, W., Schichtel, B., Kumar, N., Lowenthal, D., and Hand, J.: Revised algorithm for
762 estimating light extinction from IMPROVE particle speciation data, J Air Waste Manage, 57, 1326-1336,
763 10.3155/1047-3289.57.11.1326, 2007.

764 Qi, L., Li, Q., Henze, D. K., Tseng, H.-L., and He, C.: Sources of springtime surface black carbon in the
765 Arctic: an adjoint analysis for April 2008, Atmospheric Chemistry and Physics, 17, 9697-9716,
766 10.5194/acp-17-9697-2017, 2017.

767 Quinn, P. K., Bates, T. S., Baum, E., Doubleday, N., Fiore, A. M., Flanner, M., Fridlind, A., Garrett, T. J.,
768 Koch, D., Menon, S., Shindell, D., Stohl, A., and Warren, S. G.: Short-lived pollutants in the Arctic: their
769 climate impact and possible mitigation strategies, Atmospheric Chemistry and Physics, 8, 1723-1735,
770 10.5194/acp-8-1723-2008, 2008.

771 Ranjbar, K., O'Neill, N. T., Ivanescu, L., King, J., and Hayes, P. L.: Remote sensing of a high-Arctic,
772 local dust event over Lake Hazen (Ellesmere Island, Nunavut, Canada), Atmos Environ, 246, 2021.

773 Sand, M., Berntsen, T. K., Seland, O., and Kristjansson, J. E.: Arctic surface temperature change to
774 emissions of black carbon within Arctic or midlatitudes, Journal of Geophysical Research-Atmospheres,
775 118, 7788-7798, 10.1002/jgrd.50613, 2013a.

776 Sand, M., Berntsen, T. K., Kay, J. E., Lamarque, J. F., Seland, O., and Kirkevag, A.: The Arctic response
777 to remote and local forcing of black carbon, Atmospheric Chemistry and Physics, 13, 211-224,
778 10.5194/acp-13-211-2013, 2013b.

779 Screen, J. A. and Simmonds, I.: The central role of diminishing sea ice in recent Arctic temperature
780 amplification, Nature, 464, 1334-1337, 10.1038/nature09051, 2010.

781 Serreze, M. C. and Francis, J. A.: The arctic amplification debate, Climatic Change, 76, 241-264,
782 10.1007/s10584-005-9017-y, 2006.

783   Serreze, M. C., Barrett, A. P., Stroeve, J. C., Kindig, D. N., and Holland, M. M.: The emergence of
784   surface-based Arctic amplification, Cryosphere, 3, 11-19, 10.5194/tc-3-11-2009, 2009.
785   Sharma, S., Ishizawa, M., Chan, D., Lavoue, D., Andrews, E., Eleftheriadis, K., and Maksyutov, S.: 16-
786   year simulation of Arctic black carbon: Transport, source contribution, and sensitivity analysis on
787   deposition, Journal of Geophysical Research-Atmospheres, 118, 943-964, 10.1029/2012jd017774, 2013.
788   Shimizu, A., Nishizawa, T., Jin, Y., Kim, S. W., Wang, Z. F., Batdorj, D., and Sugimoto, N.: Evolution of
789   a lidar network for tropospheric aerosol detection in East Asia, Opt Eng, 56, 2017.
790   Shindell, D. and Faluvegi, G.: Climate response to regional radiative forcing during the twentieth century,
791   Nature Geoscience, 2, 294-300, 10.1038/ngeo473, 2009.
792   Sobhani, N., Kulkarni, S., and Carmichael, G. R.: Source sector and region contributions to black carbon
793   and PM2.5 in the Arctic, Atmospheric Chemistry and Physics, 18, 18123-18148, 10.5194/acp-18-18123-
794   2018, 2018.
795   Stohl, A.: Characteristics of atmospheric transport into the Arctic troposphere, Journal of Geophysical
796   Research-Atmospheres, 111, 10.1029/2005jd006888, 2006.
797   Stone, R. S., Dutton, E. G., Harris, J. M., and Longenecker, D.: Earlier spring snowmelt in northern
798   Alaska as an indicator of climate change, Journal of Geophysical Research-Atmospheres, 107,
799   10.1029/2000jd000286, 2002.
800   Wang, Q., Dong, X., Fu, J. S., Xu, J., Deng, C., Jiang, Y., Fu, Q., Lin, Y., Huang, K., and Zhuang, G.:
801   Environmentally dependent dust chemistry of a super Asian dust storm in March 2010: observation and
802   simulation, Atmos Chem Phys, 2018a.
803   Wang, Z., Pan, X., Uno, I., Chen, X., Yamamoto, S., Zheng, H., Li, J., and Wang, Z.: Importance of
804   mineral dust and anthropogenic pollutants mixing during a long-lasting high PM event over East Asia,
805   Environmental Pollution, 234, 368-378, 10.1016/j.envpol.2017.11.068, 2018b.
806   Warneke, C., Froyd, K. D., Brioude, J., Bahreini, R., Brock, C. A., Cozic, J., de Gouw, J. A., Fahey, D.
807   W., Ferrare, R., Holloway, J. S., Middlebrook, A. M., Miller, L., Montzka, S., Schwarz, J. P., Sodemann,
808   H., Spackman, J. R., and Stohl, A.: An important contribution to springtime Arctic aerosol from biomass
809   burning in Russia, Geophysical Research Letters, 37, 10.1029/2009gl041816, 2010.
810   Weijers, S., Buchwal, A., Blok, D., Loeffler, J., and Elberling, B.: High Arctic summer warming tracked
811   by increased Cassiope tetragona growth in the world's northernmost polar desert, Global Change Biology,
812   23, 5006-5020, 10.1111/gcb.13747, 2017.
813   Zhang, Y. L., Kang, S. C., Cong, Z. Y., Schmale, J., Sprenger, M., Li, C. L., Yang, W., Gao, T. G.,
814   Sillanpaa, M., Li, X. F., Liu, Y. J., Chen, P. F., and Zhang, X. L.: Light-absorbing impurities enhance
815   glacier albedo reduction in the southeastern Tibetan plateau, J Geophys Res-Atmos, 122, 6915-6933,
816   10.1002/2016jd026397, 2017.
817   Zwaaftink, C. D. G., Grythe, H., Skov, H., and Stohl, A.: Substantial contribution of northern high-
818   latitude sources to mineral dust in the Arctic, Journal of Geophysical Research-Atmospheres, 121, 13678-
819   13697, 10.1002/2016jd025482, 2016.

820